Free and defect-bound (bi)polarons in LiNbO₃: Atomic structure and spectroscopic signatures from *ab initio* calculations

Falko Schmidt ⬤,[*] Agnieszka L. Kozub ⬤, Timur Biktagirov ⬤, Christof Eigner ⬤, Christine Silberhorn ⬤,
Arno Schindlmayr ⬤, Wolf Gero Schmidt ⬤, and Uwe Gerstmann ⬤
Department Physik, Universität Paderborn, 33095 Paderborn, Germany

Polarons in dielectric crystals play a crucial role for applications in integrated electronics and optoelectronics. In this work, we use density-functional theory and Green's function methods to explore the microscopic structure and spectroscopic signatures of electron polarons in lithium niobate (LiNbO₃). Total-energy calculations and the comparison of calculated electron paramagnetic resonance data with available measurements reveal the formation of bound polarons at Nb_{Li} antisite defects with a quasi-Jahn-Teller distorted, tilted configuration. The defect-formation energies further indicate that (bi)polarons may form not only at Nb_{Li} antisites but also at structures where the antisite Nb atom moves into a neighboring empty oxygen octahedron. Based on these structure models, and on the calculated charge-transition levels and potential-energy barriers, we propose two mechanisms for the optical and thermal splitting of bipolarons, which provide a natural explanation for the reported two-path recombination of bipolarons. Optical-response calculations based on the Bethe-Salpeter equation, in combination with available experimental data and new measurements of the optical absorption spectrum, further corroborate the geometries proposed here for free and defect-bound (bi)polarons.

I. INTRODUCTION

Lithium niobate (LiNbO₃, LN) is a dielectric material with many technical applications that exploit its large acousto-optical, piezoelectric, electro-optical, and nonlinear optical coefficients. In particular, it is widely used in optical sensors [1], advanced gas sensors [2], waveguides [3], optical modulators [4], and integrated electronics and optoelectronics [5].

The composition of typical LN crystals for commercial purposes, grown with the Czochralski method, is not stoichiometric but congruent with a Li:Nb ratio of around 48.5:51.5 [6]. The defects resulting from the Li deficiency strongly influence the optical properties of the material [7–9]. Amongst others, they increase the phase-matching angle and the extraordinary refractive index, while the birefringence decreases [10]. Point defects can also act as seeds for electron polarons, which impact many applications: On the one hand, they may reduce the conversion efficiency and the lifetime for frequency conversion [11]. On the other hand, polarons enable exciting new applications, including three-dimensional real-time holographic displays. Since different types of polarons coexist, holograms with multiple colors may be recorded in this way [11,12]. This study aims at a microscopic understanding of electron polarons and their spectroscopic properties.

The basic stacking sequence of ferroelectric LN crystals in the absence of native defects is illustrated in Fig. 1(a). The prevalent model discussed in the literature [13,14] states that the free polaron is an excess electron weakly bound to a Nb atom at a regular lattice site, labeled Nb_{Nb}. The self-trapped electron gives rise to an optical absorption band around 0.9 eV [14]. In contrast, excess electrons trapped at point defects may induce further lattice relaxation and form bound polarons or bipolarons. The bound polaron is believed to be an excess electron at a Nb_{Li} antisite defect, shown in Fig. 1(b), which leads to an optical absorption band around 1.7 eV [14]. The bipolaron, finally, is formed by a pair of bound excess electrons, one at a Nb_{Li} antisite defect and the other at the neighboring regular Nb_{Nb} atom, giving rise to an optical absorption band around 2.5 eV [14].

Although point defects are indispensable to properly describe congruent, i.e., Li-deficient, LiNbO₃, it is still not conclusively established which kinds of defects occur in which concentrations. While oxygen vacancies are practically excluded [15–18], different cation-substitution models are possible [19]. Seemingly, the simplest way to achieve the observed Li:Nb ratio, originally proposed by Lerner *et al.* [17], is given by Nb_{Li} antisite defects, where a Li atom is substituted by a Nb atom as shown in Fig. 1(b). However, a Li deficiency can also be caused by Li vacancies or Nb interstitials. A combination of the latter was proposed by Zotov *et al.* [19]: In Fig. 1(c), we display such a Nb_V-V_{Li} pair consisting of a Nb interstitial and a Li vacancy located in adjacent octahedra. As will be shown later, this defect can also be interpreted as a metastable form of a Nb_{Li} antisite, where the antisite atom is shifted into the neighboring empty octahedron.
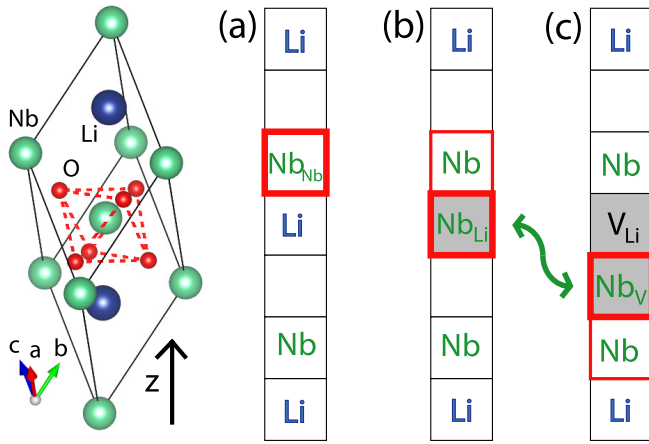
---

[*]schmidtf@mail.upb.de

FIG. 1. (Left) Rhombohedral unit cell of ideal stoichiometric LiNbO$_3$ containing ten atoms (two formula units). Large blue, large green, and small red balls represent Li, Nb, and O atoms, respectively. The dotted lines indicate an oxygen octahedron. (Right) Schematic representation of the stacking sequence of (a) defect-free LN, (b) LN with a Nb$_{Li}$ antisite, and (c) LN with a Nb$_V$-V$_{Li}$ defect pair. Each square represents an oxygen octahedron that can be either empty or filled with an Nb or Li atom. Gray squares highlight deviations from the ideal bulk crystal, while red frames mark the formation regions of polarons (thick lines) and bipolarons (thick plus thin lines). The arrow indicates the transition from the regular antisite (b) to the defect pair (c), where the antisite Nb atom shifts into a neighboring empty octahedron.

The bipolaron can be split into a free and a bound polaron, either thermally [14] or by illumination [11]. The single polarons, especially the free polarons, are bound to a lesser extent; they can easily move through the crystal and recombine at a different atomic site. In the case of light-induced splitting, this recombination typically occurs in dark regions where the illumination is blocked, for example, by a mask [20]. In a pump-probe experiment, Herth *et al.* [21] found that the light-induced absorption of LiNbO$_3$, which should involve both free and bound polarons, features only one band centered around 1.6 eV, however. This suggests that free polarons, which are not detected, are either not created during the breakup of the bipolarons or fall into a deeper defect level before detection. In a similar study, on the other hand, Merschjann *et al.* [22] reported a two-component decay, which they attributed to the presence of two recombination paths. While they related the fast decay to a direct recombination via mobile free polarons, the slow process was tentatively attributed to a two-step process, where free polarons are temporarily trapped by ionized polarons before recombining with optically active polarons.

Free as well as bound polarons are candidates for being observable in electron-paramagnetic-resonance (EPR) experiments, as both contain unpaired electrons. Early EPR experiments for LN by Schirmer and von der Linde [23] indicated the presence of an Nb-related defect center with axial symmetry, which they attributed to an electron self-trapped at a Nb lattice site, i.e., to a Nb$^*_{Nb}$ free polaron. Later, the same EPR signal was reattributed to a bound polaron at a Nb$_{Li}$ antisite defect [24], possibly adjacent to a Li vacancy [25]. The observation that the EPR signal disappears for high

doping concentrations of Mg [24] supports this interpretation, because the Mg atoms are assumed to occupy Li sites and thus to prevent the formation of Nb$_{Li}$ antisites [26], which are supposed to give rise to bound rather than free polarons [14]. However, the most striking argument for this scenario is the fact that the optical absorption at 1.7 eV and the EPR signal anneal simultaneously in the temperature range of 100–200 K, suggesting bound polarons as a common origin [27].

While it now seems clear that Nb antisite atoms in the Li sublattice are involved in the creation of polarons and bipolarons, there is uncertainty at which point defects they form precisely, with several models under discussion [17–19,28,29]. Friedrich *et al.* [30] examined the optical properties of, amongst others, the Nb$_{Li}$ antisite and the Nb$_V$-V$_{Li}$ defect pair for polarons and bipolarons within time-dependent density-functional theory (TDDFT). For the polaron, they found both defect types to reproduce the absorption at 1.7 eV equally well, whereas the Nb$_{Li}$ antisite fails to account for the absorption band at 2.5 eV ascribed to the bipolaron. Unfortunately, the predictive power of these TDDFT calculations is limited, because they accurately redistribute oscillator strength between optical transitions but do not shift the excitation energies themselves [31]. Therefore, empirical corrections must be applied to describe materials like lithium niobate with large electron-hole binding energies.

In this work we go beyond previous studies by (i) presenting calculated EPR data for different defect types, (ii) discussing the energetics of relevant point defects as well as their transformation based on the Slater-Janak approach, and (iii) eliminating the need for empirical parameters in the optical-response calculations by solving the Bethe-Salpeter equation (BSE) in combination with a quasiparticle band structure corrected by the G_0W_0 approximation for the electronic self-energy. In addition, we measure the optical absorption spectrum of congruent LN in the energy region relevant for (bi)polarons.

This paper is organized as follows. After an outline of the computational methods and the experimental setup in Sec. II, different structural models for the polarons are examined. In Sec. III A, we determine the defect formation energies for the various defect types and the stability of charge states associated with polarons and bipolarons. Our calculations of the EPR parameters in Sec. III B confirm a quasi-Jahn-Teller distorted, i.e., tilted ground-state, structure for the bound polaron. In Sec. III C, the calculated optical-response functions are compared with the experimental data as well as earlier measurements. Finally, Sec. IV summarizes our conclusions.

II. METHODS

A. Computational approach

The defect structures are optimized with the QUANTUM ESPRESSO [32] package, a plane-wave pseudopotential implementation of density-functional theory (DFT). The defects are embedded in periodically repeated supercells. We use norm-conserving pseudopotentials and a cutoff of 85 Ry for the kinetic energy in the plane-wave basis set. The description of electronic exchange-correlation effects is based on the PBEsol functional [33], which yields very precise lattice parameters

for LN [34] as well as related materials [35,36]. Following Nahm and Park [37], we also add Hubbard U parameters within a DFT $+ U$ scheme [38] for an accurate modeling of the strongly localized Nb $4d$ orbitals. The U values used here are not treated as empirical parameters but calculated self-consistently for every Nb atom. We obtain a value of 5.2 eV for the Nb_{Li} antisite atom and the Nb_V interstitial atom in this way, while the U values for the other Nb atoms, including Nb^*_{Nb} atoms with free polarons, are about 4.7 eV. In the latter case (free polarons), the Hubbard U is even essential to describe the self-trapping of electrons, because semilocal exchange-correlation functionals like PBEsol fail to relax into the strongly distorted configurations required for the localization of the excess electron. All structures used in the following to evaluate the spectroscopic fingerprints of (bi)polarons are hence optimized with the PBEsol $+ U$ approach.

The rhombohedral unit cell of ideal stoichiometric LN contains ten atoms and is displayed in Fig. 1. The oxygen atoms form octahedra that may be occupied by Li and Nb cations. Along the [111] direction, this leads to the periodic stacking order of cations and empty octahedra previously shown in Fig. 1(a). The cations, Li more than Nb, are in fact not localized in the center of the octahedra but shifted along the crystal z axis (see Fig. 1). As a consequence, they approach the faces of their own octahedra, moving closer to the adjacent empty octahedra, and thus cause the ferroelectricity of the material [24].

To model point defects in LN, we use the experimental lattice parameters [39], which are nearly perfectly reproduced by the PBEsol functional [34], but perform a full internal optimization of the atomic positions inside the unit cell. From the 10-atom rhombohedral unit cell, we construct supercells with 80 atoms (for standard optical-response calculations) and up to 270 atoms (for benchmarking) that accommodate individual point defects together with their crystal environment. The structures are relaxed using a shifted $2 \times 2 \times 2$ Monkhorst-Pack **k**-point mesh. We use convergence thresholds of 10^{-4} Ry and 10^{-8} Ry/Bohr for energies and forces, respectively.

While bipolarons in LN (charge state $+2$) are diamagnetic, free (-1) and bound $(+3)$ polarons constitute paramagnetic states with a single unpaired electron and spin $S = 1/2$. Therefore, the latter two are candidates to explain the observed Nb-related EPR signal. In order to identify the actual underlying defect structures, we calculate the full set of EPR parameters, i.e., the hyperfine tensors [40] as well as the elements of the electronic g tensor [41,42], for a set of possible defect models. For this purpose, we use the gauge-including projector-augmented-wave (GIPAW) part of the QUANTUM ESPRESSO package [32,43]. Here and for all other calculations, scalar-relativistic, norm-conserving GIPAW pseudopotentials are employed to evaluate the linear response of the polarons to an external magnetic field [41,44]. Spin-orbit coupling, which causes the deviation of the g tensor from the free-electron value 2.002 319, is taken into account assuming perfect spin-alignment along the applied magnetic field. We find that the hyperfine interaction obtained for the supercells containing 80 and 270 atoms coincides within 2%. This confirms that the charge-density distribution of the optically active unpaired electron is already sufficiently well described in the 80-atom

cell, giving us confidence that this supercell is also well suited for the computationally demanding $G_0W_0 +$ BSE calculation of the optical absorption spectra in Sec. III C. This applies also to the case of bipolarons, where the structural relaxations are larger but still restricted to the immediate neighborhood of the defect atoms. In fact, a recent investigation [30] of this class of defects showed only minor differences for supercells containing either 80 or 270 atoms.

In order to take the charge compensation by other defects into account, we analyze the formation energies of the polaronic defects in their various charge states n as a function of the chemical potential, i.e., the Fermi level. The charge-transition levels, defined as the values of the chemical potential where the charge states of minimum energy change, are obtained from the Slater-Janak (SJ) transition states, defined by $(n/n + 1) \approx \epsilon_{HOMO}(n + \frac{1}{2})$ (highest occupied molecular orbital, HOMO) [45,46]. For this purpose, the defects under investigation are half-integer charged from $+0.5$ to $+3.5$ and then fully relaxed to account for the influence of symmetry-lowering Jahn-Teller distortions. As recently demonstrated for LN [47], the concept of SJ transition states entails relatively small error bars, while charge corrections, necessary when comparing total energies of systems with different numbers of electrons, are avoided. To allow for a direct comparison with experimental data, we follow Ref. [9] and apply the Heyd-Scuseria-Ernzerhof (HSE) hybrid functional [48] when evaluating the SJ transition states, which results in an electronic band gap of 5.39 eV that is in excellent agreement with the quasiparticle gap of 5.4 eV obtained using significantly more expensive Green's function techniques [49].

The optical-response function is calculated by solving the Bethe-Salpeter equation based on quasiparticle band structures, which include self-energy corrections within the G_0W_0 approximation [50], and PBEsol $+ U$ wave functions. A similar approach was previously shown to excellently reproduce the optical absorption spectrum of defect-free stoichiometric $LiNbO_3$, which is characterized by strong quasiparticle effects and large electron-hole binding energies [49,51], and has also been successfully applied to other alkali-metal niobates [52]. Technically, we employ the YAMBO package [53] within the plasmon-pole approximation [54] for the G_0W_0 calculation. In this step, 800 electronic energy bands are included along with a block size of 7 Ry for the response function and a damping parameter of 0.15 eV. For computational reasons, the number of bands included in the solution of the BSE is reduced to 96 (36) regular valence bands, the defect bands, and 84 (44) conduction bands for the screening (the BSE kernel). We confirmed that this reduction does not impair the spectrum up to the onset of the LN bulk optical transitions; i.e., it does not affect the accuracy of the defect-state signatures inside the band gap that are relevant here. For all optical calculations in the $2 \times 2 \times 2$ supercell (with 80 atoms), a shifted $2 \times 2 \times 2$ **k**-point mesh is used, corresponding to a $4 \times 4 \times 4$ mesh in the single 10-atom unit cell. In the inset of Fig. 2, we show that this choice ensures convergence of the optical spectra with respect to the **k**-point sampling. The underlying PBEsol $+ U$ band structure is calculated using QUANTUM ESPRESSO both with and without spin polarization. The symmetric spin splitting $\Delta\epsilon_{spin}$ of the
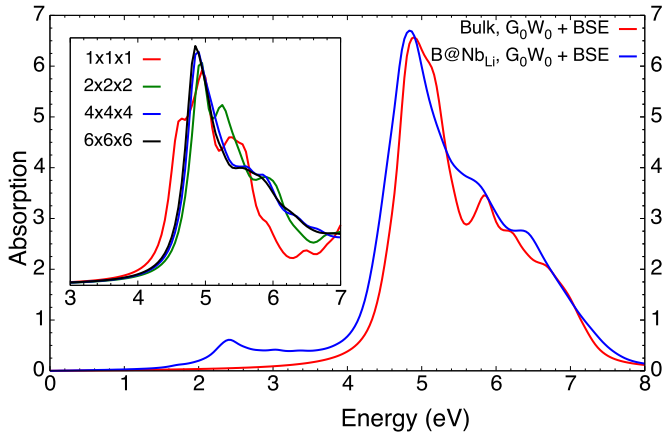
FIG. 2. Optical absorption spectra of stoichiometric $LiNbO_3$ (red line) and $LiNbO_3$ with a bipolaron at a Nb_{Li} antisite defect (blue line), both in the 80-atom supercell. The inset shows the convergence with respect to the **k**-point sampling for the 10-atom unit cell of the defect-free material. Note that a $4 \times 4 \times 4$ **k**-point set for the 10-atom unit cell is equivalent to a $2 \times 2 \times 2$ set for the larger 80-atom supercell.

defect-related gap levels is subsequently used to shift the defect peaks in the optical spectra, which are initially derived with no spin polarization, by $\Delta\epsilon_{spin}/2$. This approximation is justified because the conduction bands are almost unaffected by the spin polarization. This is shown in Fig. 2, where we compare the defect-free crystal (red line) with a defect-containing cell (blue line): While the introduction of the defect gives rise to a peak around 2.5 eV, the main absorption features above 4 eV are essentially identical. As a consequence, the spin splitting effectively translates into a shift of the initial state (occupied defect level) with respect to the final state (empty conduction bands) in the optical transition.

B. Experimental setup

The present theoretical work is accompanied by a brief experimental analysis of the optical response of $LiNbO_3$. For this analysis, we use a *z*-cut sample grown by Crystal Technology [55]. The wafer composition is congruent within 0.02 mol% Li_2O with a typical compositional uniformity better than ± 0.005 mol% Li_2O. The $+z$ side and the $-z$ side are optically polished and cleaned in a process containing acetone, ethanol, water, and ammonium to remove any residual materials from the surface. We measure the transmission spectrum between 350 and 800 nm using a standard spectrometer (Agilent Carry 5000). The wavelength step is set to an interval of 0.1 nm and a signal-to-noise ratio of 2000. To eliminate interference fringes induced by the birefringence, we perform the measurements along the *z* direction, using light polarized in the *xy* plane that is only affected by the ordinary refractive index n_o. This allows for an increased signal-to-noise ratio, because n_o and n_e are precisely aligned to the crystallographic axes, and no linear polarizer is required in this case. The measurements are performed at room temperature using a 5-mm iris in the spectrometer. To further increase the signal-to-noise ratio, we measure the bright and the dark spectrum of the spectrometer separately beforehand. Subsequently, we correct the

TABLE I. Calculated charge-transition levels in eV for the Nb_{Li} antisite and the Nb_V-V_{Li} defect pair calculated via fully relaxed Slater-Janak transition states using either PBEsol $+ U$ or the HSE hybrid functional. The values in brackets indicate the creation of free polarons far away from the defect center.

	PBEsol $+ U$		HSE	
Fundamental gap:	3.42		5.39	
Charge transition	Nb_{Li}	Nb_V-V_{Li}	Nb_{Li}	Nb_V-V_{Li}
(+4/+3)	3.09	3.15	4.36	4.48
(+3/+2)	3.25	2.69	4.56	4.09
(+2/+1)	(3.13)	(3.28)	(4.52)	(4.74)
(+1/0)	(3.04)	(3.11)	(4.63)	(4.50)

transmission spectra for Fresnel reflections at both end facets. The raw data are measured in wavelength vs transmission; from these data, we calculate the absorption in dependence of the energy, resulting in an absorption spectrum covering the highly relevant range between 1.5 and 3.5 eV.

III. RESULTS AND DISCUSSION

A. Formation energies and charge-transition levels

We start by investigating the defect energetics, or more precisely the total-energy differences required for the formation of polarons in their various charge states. While formation energies for the Nb_{Li} antisite defect in LN were already reported [47,56], the Nb_V-V_{Li} defect pair was discussed in Ref. [19,30], but its thermodynamic properties, such as the charge-transition levels, have not been explored in detail. Therefore, here we calculate the defect formation energies for both defect types using identical procedures and discuss their structural similarity and relative stability in dependence of the Fermi level. Table I shows our results for the charge-transition levels, calculated directly by means of the Slater-Janak transition states. We note that their relative positions turn out to be robust with respect to the choice of the exchange-correlation functional. Compared to PBEsol $+ U$, the values obtained with the HSE hybrid functional are higher by about 1.35 eV, reflecting the larger fundamental band gap, which is underestimated by PBEsol $+ U$. The PBEsol $+ U$ value of 3.42 eV is still in line with a recent local-density-approximation study yielding a band gap of 3.54 eV [57], while the HSE band gap of 5.39 eV is very close to a G_0W_0 study yielding 5.40 eV [51]. In the following, we hence base our discussion on the HSE values, which are expected to be directly comparable with experiments. The dependence of the defect formation energies on the Fermi level can be inferred from the calculated charge-transition levels and is illustrated in Fig. 3.

Our results show that the defect formation energies of the various charge states intersect in a rather small energy range, especially in the case of the isolated Nb_{Li} antisite. This makes their evaluation challenging and requires a high numerical accuracy, as small deviations may interchange the relative stability of different charge states. In this respect, the concept of fully relaxed Slater-Janak transition states plays out its strength. For the Nb_{Li} antisite, our values are similar to those reported in Ref. [9], coinciding within 0.3 eV. Nonetheless,

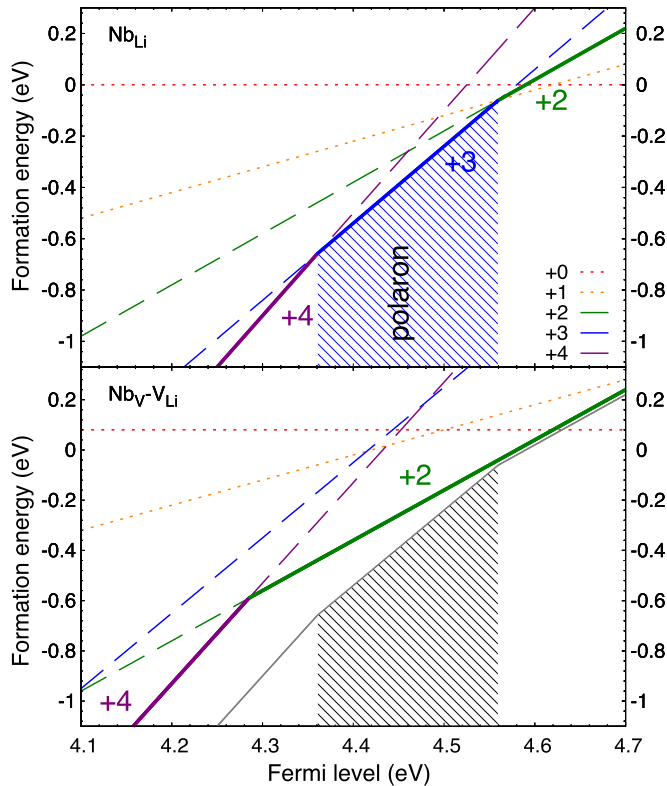FIG. 3. Defect formation energies for the Nb_{Li} antisite (top) and the Nb_V-V_{Li} defect pair (bottom) in various charge states obtained with the HSE hybrid functional. The line crossings define the charge-transition levels. For a given Fermi level, the state with the lowest formation energy (solid line) is the thermodynamically stable one. The $+1$ and the 0 charge state involve the creation of one and two separate free polarons, respectively, and are not actual defect-related states. For better comparison, the stable charge states ($+4$, $+3$, $+2$) of the Nb_{Li} antisite (top) are repeated in the lower figure, illustrating that the $+2$ (bipolaron) charge states for the two defects are almost degenerate.

our results provide some additional insight that applies to both defect types, the antisite as well as the Nb_V-V_{Li} defect pair.

(i) In the $+3$ charge state, which corresponds to bound polarons, both defect types undergo a symmetry-lowering quasi-Jahn-Teller distortion, where the Nb atom moves away from the threefold symmetry axis along two of the rhombohedral axes, effectively tilting the charge density of the polaron. The total energy is thus lowered by 43 and 38 meV for Nb_{Li} and Nb_V-V_{Li}, respectively. We estimate the energy barrier between the three equivalent tilted configurations to be even lower, so that a dynamic Jahn-Teller effect becomes possible at room temperature, resulting in thermally averaged, essentially axially symmetric spectroscopic fingerprints. In contrast, for the $+2$ charge state associated with the bipolarons, only the axial geometry is possible, because the two excess electrons act as a covalent bond between the two neighboring niobium atoms that stabilizes the axial symmetry.

(ii) For Nb_{Li}, the bound polaron is not subject to a negative-U effect but predicted to be thermodynamically stable for Fermi levels in a small window around 4.45 eV. For Nb_V-V_{Li}, on the other hand, the polaron experiences a

negative-U effect, which results in a direct ($+4/+2$) transition at 4.29 eV and prevents its observation in the dark. This reflects the strong structural relaxation due to the trapped polaronic charges and implies that optical excitation is necessary for experimental detection.

(iii) In the case of the $+1$ and 0 charge states, a wave-function analysis reveals that the extra electrons are in fact not bound to the defect but instead produce separate free polarons far away from the defect center. Therefore, the calculated charge-transition levels actually belong to the $(0/-)$ transitions of free polarons and do not refer to defect-related bound polarons. For this reason, we apply the notation $+1 = +2^*$ and $0 = +2^{**}$ and leave these states out of the following discussion. In Fig. 3, they are hence not considered as stable charge states of the defects.

Figure 4 illustrates all models considered here together with the relevant optically active charge densities. For the structures involving a Nb_V-V_{Li} defect pair, the Li atom in the uppermost oxygen octahedron displayed in the figure moves into the empty octahedron immediately below, which renders the local electronic configurations around the regular Nb_{Li} antisite defect and the defect pair nearly equivalent. This is most obvious in the case of bipolarons illustrated in Figs. 4(g) and 4(h), where the partial charge densities are almost identical. It underlines the close relationship between the two defect types, which can thus be interpreted as variations of each other or even as a single bistable defect type. They differ insofar as the nearest Li neighbor, the uppermost (lowermost) displayed Li atom for the antisite (defect pair), is located at a different distance from the bipolaron, however, and relaxes back to this stable position even if displaced into the adjacent empty octahedron. Several studies have already found evidence for similar transformations involving regular Li atoms even at room temperature [58], but more frequently at higher temperatures [39,59]. As Li and Nb have similar ionic radii [60] and mean thermal displacements [61], it is very likely that an antisite Nb atom can also jump into a neighboring empty oxygen octahedron.

Figure 5 shows the microscopic neighborhood of the relaxed defects considered in this work. Apparently, the relaxation of the oxygen atoms is mostly restricted to a movement within the respective O layer. This supports the simple picture that the crystal structure is built up by oxygen octahedra, which are filled by Li and Nb cations flexible in position and relative distances (see Fig. 1). In the case of bound (bi)polarons, the Nb antisite atoms and their closest Nb neighbors are strongly shifted along the z axis by up to 0.6 Å. The resulting shift of the Nb sublattice relative to the oxygen cages suggests relevant implications for the macroscopic polarization of the material [62]. In the case of free polarons, this shift of the Nb sublattice is absent, and the most prominent feature of the relaxation is an outward relaxation of the six oxygen neighbors. Although these shifts are smaller than 0.1 Å, they are essential for the trapping of the excess electron. Oxygen neighbors are also crucial for the tilted ground-state configurations of the free and bound polarons, where a distortion of the central O cage takes place. While the influence of this distortion onto the position of the central Nb atoms is rather small, the spatial distribution of the polaron charge is strongly affected, changing from an axially oriented dumbbell
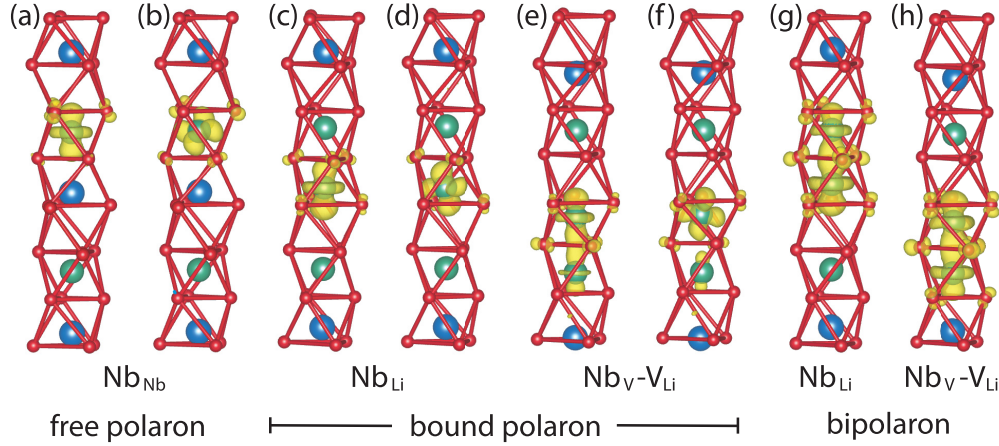
FIG. 4. Partial charge densities (highest occupied orbital) of the defect state for the free polaron (a, b), the bound polaron at a Nb_{Li} antisite defect (c, d) and a Nb_V-V_{Li} defect pair (e, f), and the bipolaron at Nb_{Li} (g) and Nb_V-V_{Li} (h). Figures (b), (d), and (f) refer to tilted configurations, while the other structures exhibit axial symmetry. As in Fig. 1, large blue, large green, and small red balls represent Li, Nb, and O atoms, respectively. The charge density of the electron (bi)polarons is always predominantly localized at Nb atoms. For the bipolarons, it also encompasses the nearest regular Nb atom of the crystal lattice.

to a tilted clover-leave shape that reflects the nature of the respective highest occupied Nb 4*d* orbital.

Experimentally, it is well established that polarons and bipolarons can be transformed into each other [14]. In particular, the splitting of bipolarons has been demonstrated both optically by short intense laser pulses with a wavelength of 532 nm [22] and thermally with a bipolaron dissociation energy of 0.27 eV [63]. In the following, we show that a scenario of bipolarons or polarons related to a structural transformation is in full agreement with these observations. As illustrated in Fig. 6, this structural transformation is driven by the antisite Nb atom, which causes a transition between the Nb_V-V_{Li} (top left) and the Nb_{Li} antisite (top right) configuration by passing through the oxygen layer (top center).
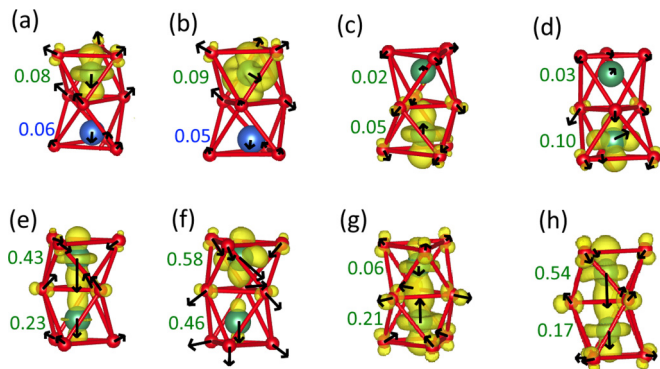

FIG. 5. Atomic shifts from the ideal lattice positions (arrows indicate direction and size) for the free polaron (a, b), the bound polaron at a Nb_{Li} antisite defect (c, d) and a Nb_V-V_{Li} defect pair (e, f), and the bipolaron at Nb_{Li} (g) and Nb_V-V_{Li} (h). Panels (b), (d), and (f) refer to tilted configurations, while the other structures exhibit axial symmetry. For the central Nb (large green balls) and Li atoms (large blue balls), the shift is also given explicitly in Å; small red balls represent O atoms. The charge density of the HOMO is also displayed again.
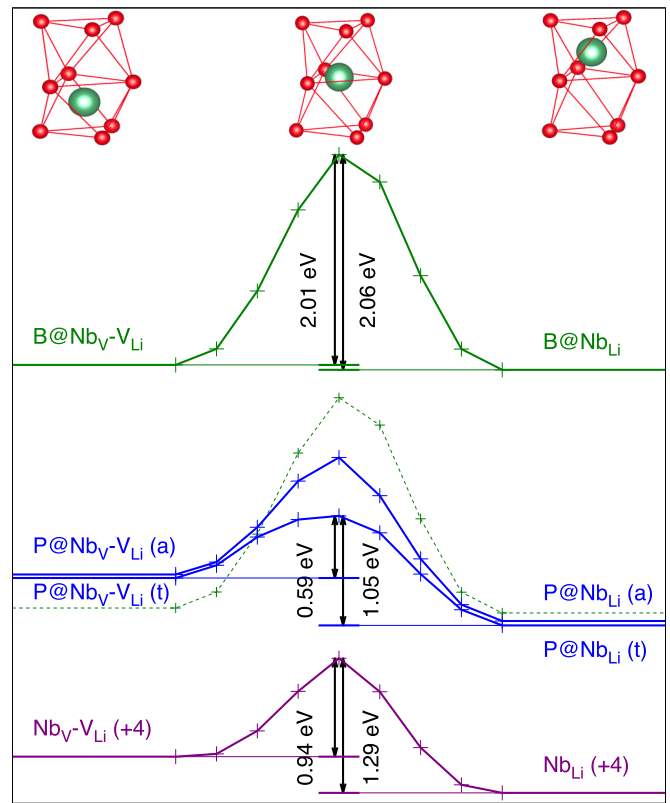

FIG. 6. Energy barriers obtained with the PBEsol + *U* functional for the transition between the Nb_V-V_{Li} defect pair (left) and the Nb_{Li} antisite (right) as the Nb atom passes through the oxygen layer (center). The curves show the +2 bipolaron (B) charge state (green line), the +3 polaron (P) state in the axial (a) and tilted (t) symmetry (blue line), and the fully ionized +4 charge state (purple line). The dashed green line indicates the position of the bipolaron relative to the polaron for a Fermi level of 4.45 eV, corresponding to the center of the energy window where both the bipolaron at the defect pair and the polaron at Nb_{Li} are predicted to be thermodynamically stable.

For the bipolarons (charge state $+2$), we find an energy barrier of approximately 2.0 eV in both directions. This value is much too large for a direct thermal dissociation, but an excitation into the conduction bands, either thermally or optically (see Sec. III C), remains a possible scenario. Judging from the energetic position of the charge-transition levels around 1.4 eV below the conduction bands, thermal ionization via the conduction bands seems less probable even if we apply a simple two-electron picture and allow for a factor-of-2 reduction.

A purely thermal dissociation of bipolarons appears to require a more complicated multistep mechanism. In this context, we note that, for polarons (charge state $+3$), there is a much lower barrier of 1.05 eV for the axial symmetry, which is further reduced to 0.59 eV for the tilted ground-state configuration, as seen in Fig. 6. Therefore, we propose the following mechanism for the thermal splitting of bipolarons at the Nb_V-V_{Li} defect pair. First, the bipolaron undergoes a charge transition to the $+3$ charge state. Assuming a Fermi level of 4.45 eV, which corresponds to the center of the energy window where regular Nb_{Li} polarons are predicted to be stable, this amounts to a thermally activated excitation of 0.37 eV according to Fig. 3. Second, the polaron in the axial symmetry relaxes into the tilted configuration with a minor barrier clearly below 30 meV. Third, the Nb atom only has to overcome a barrier with an upper bound of 0.59 eV for the transition to the bound-polaron state at the regular Nb_{Li} antisite. This is in reasonable agreement with the experimentally observed value of 0.27 eV [63], keeping in mind that we neglect barrier-lowering effects of phonons and entropy in this estimate. A recent study [64] showed that these effects are small but not negligible in the case of Au nanowires on a Si step.

The bistability of the Nb antisite defect also provides a natural explanation for the experimentally observed two-path recombination of the bipolarons. Whereas the fast process is most probably due to a direct recombination with free polarons, we speculate that the slow process involves a more time-consuming structural transformation between Nb_{Li} and Nb_V-V_{Li}.

B. Electron paramagnetic resonance

We now discuss the experimentally observed electron paramagnetic resonance spectra in the light of the total-energy calculations. For this purpose, we calculate the EPR parameters for the free polaron (FP) localized at a regular Nb^*_{Nb} lattice site as well as for the bound polaron at the antisite defect (P@Nb_{Li}) and at the defect pair (P@Nb_V-V_{Li}), all within the axial and the tilted configuration. Although the potentially EPR-active polaron charge state of the Nb_V-V_{Li} defect pair experiences a negative-U effect, it cannot be ignored, because experimental EPR spectra may be observed upon illumination exclusively.

The calculated g tensors for the paramagnetic bound polarons (charge state $+3$) and free polarons (charge state -1) are summarized in Table II. As the calculated and measured tensors reflect the symmetry of the defect configurations, the models for the axial and tilted structures can be naturally attributed to the experimental data sets from Refs. [23] and [25], respectively. While both studies were performed at rather low temperatures around 20 K, the spectrum in Ref. [23]

TABLE II. Principal values of g tensors and axial anisotropy $\Delta g = g_{zz} - (g_{xx} + g_{yy})/2$ for free polarons (FP) at Nb^*_{Nb} and for bound polarons at antisites (P@Nb_{Li}) and at defect pairs (P@Nb_V-V_{Li}), with axial and tilted symmetry. The values are calculated (PBEsol) for the PBEsol $+ U$ relaxed structures and compared to experimental data from Refs. [23,25].

Model	g_{xx}	g_{yy}	g_{zz}	Δg
FP (axial)	1.923	1.923	1.986	0.063
P@Nb_V-V_{Li} (axial)	1.820	1.820	1.986	0.166
P@Nb_{Li} (axial)	1.806	1.806	1.983	0.177
Expt. [23]	1.72	1.72	1.90	0.18
FP (tilted)	1.932	1.927	1.959	0.029
P@Nb_V-V_{Li} (tilted)	1.816	1.844	1.959	0.129
P@Nb_{Li} (tilted)	1.773	1.871	1.954	0.132
Expt. [25]	1.709	1.795	1.883	0.131

has a lower resolution, so that the actual nonaxial (tilted) symmetry was only discovered much later in Ref. [25]. As a consequence, the earlier spectrum was instead interpreted assuming an axial symmetry [23].

At first view, all defect models for the bound polaron agree fairly well with the experimental data. Those for free polarons, however, yield much too small g tensor anisotropies Δg (e.g., 0.06 instead of 0.18). The driving force behind the g tensor is spin-orbit coupling [44,65]; without spin-orbit coupling, the resulting g values will always reproduce the free-electron value of about 2.002 319. The significant deviation for free polarons, in particular with respect to the anisotropy Δg, means that the spin density (the density of the unpaired electron, i.e., the polaron) does not reflect the correct spatial distribution. At first view, having in mind the strong similarity of the polaron density for the free and bound polarons (see Fig. 4) this result might appear surprising. However, a closer look at the densities in Fig. 5 shows that the spin-density distribution at the neighboring oxygen atoms is qualitatively different: While the spin density for the bound polarons is nearly equally distributed over all six O neighbors, for the free polaron we find a substantial spin density only at the three O neighbors with larger distances to the adjacent Li atom. As the p-like electrons of the oxygen atoms strongly contribute to the spin-orbit coupling, this difference is relevant for the calculated g-tensor anisotropies. As a consequence, free polarons in the axial as well as the tilted geometry have to be ruled out: They are not involved in the experimentally observed EPR spectra.

Table III shows results for the anisotropic part of the hyperfine tensor for all considered models in their paramagnetic states. For these quantities, the differences between the various models are much larger than those for the g tensor. The high-resolution experiments by Müller and Schirmer [25] exhibit a large deviation between T_{xx} and T_{yy}, which is best matched by the polaron at the Nb_{Li} antisite defect in the tilted configuration. In contrast, the earlier experimental values by Schirmer and von der Linde [23] assume a defect with axial symmetry. Consequently, they are best reproduced by the antisite polaron in the axially symmetric configuration.

From both the g tensor and the anisotropic dipole part of the hyperfine tensor, we conclude that bound polarons at Nb_{Li}

TABLE III. Principal values in MHz of the anisotropic part of the ^{93}Nb-related hyperfine tensor for free polarons (FP) at Nb^*_{Nb} and for bound polarons at antisites (P@Nb_{Li}) and at defect pairs (P@Nb_V-V_{Li}), with axial and tilted symmetry. For the experimental values from Refs. [23,25] only relative signs are available.

Model	T_{xx}	T_{yy}	T_{zz}
FP (axial)	−102.3	−102.3	+204.6
P@Nb_V-V_{Li} (axial)	−96.7	−96.7	+193.3
P@Nb_{Li} (axial)	−109.6	−109.6	+219.2
Expt. [23]	±120	±120	∓240
FP (tilted)	+108.1	+108.5	−216.6
P@Nb_V-V_{Li} (tilted)	+107.1	+121.5	−228.6
P@Nb_{Li} (tilted)	+94.9	+135.9	−230.8
Expt. [25]	±77.7	±170.7	∓248.3

antisite defects are responsible for the EPR signature related to the optical absorption band around 1.7 eV. This is in line with Schirmer *et al.* [24], who proposed the bound polaron located at the antisite as the source of the EPR signal, but our results yield additional information about the defect structures: It is the energetically more favorable tilted configuration that is able to reproduce the experimentally measured, well-resolved EPR parameters determined in Ref. [25].

C. Optical absorption spectra

In this section, we combine theoretical calculations and experimental measurements in order to elucidate the polaron contribution to the optical absorption spectrum of congruent LN. To illustrate our computational approach, Fig. 7 displays the absorption spectrum for the bipolarons at Nb_V-V_{Li} defect pairs calculated at different levels of theory. In order to allow a direct comparison with the experimental data, the incident
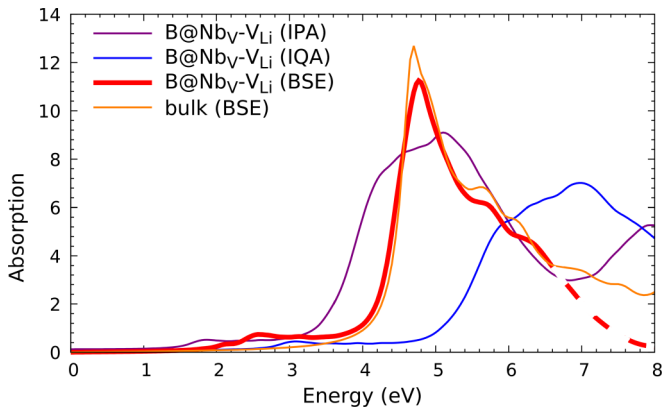

FIG. 7. Absorption spectrum of LiNbO$_3$ with a bipolaron at the Nb_V-V_{Li} defect pair (B@Nb_V-V_{Li}), calculated for the 80-atom supercell at different levels of theory. For comparison, the BSE spectrum for the ideal defect-free bulk material (10 atom cell) is also shown. For the BSE calculation in the defect-containing cell, a calculation of the standard number of empty states (539) is prohibitively expensive and has to be reduced to 84 (44) for the screening (BSE kernel). As a consequence, high-energy transitions above 6 eV are no longer included, resulting in a too fast decrease of the spectrum (dashed line).
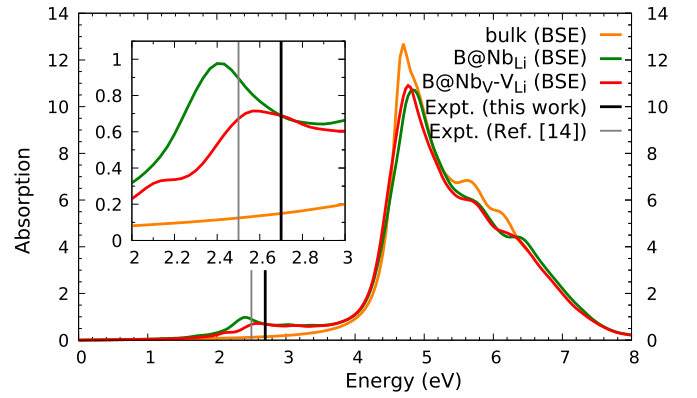

FIG. 8. Absorption spectrum of LiNbO$_3$ with a bipolaron at a Nb_{Li} antisite (green line) and a Nb_V-V_{Li} defect pair (red line). The bulk spectrum (orange line) is added for comparison. All spectra are calculated taking into account transitions into 84 (44) empty states for the screening (BSE kernel). The vertical lines correspond to the center of the experimentally observed absorption bands from this work (black line) and Ref. [14] (gray line).

light is assumed to be linearly polarized in the *xy* plane. While the spectra obtained for light polarized in the *x* and *y* directions are identical in the case of axial symmetry, we use the average of the two spectra for the tilted configurations. Within the independent-particle approximation (IPA), the optical response is directly derived from the PBEsol + U wave functions and transition energies. The absorption energy of the bipolarons, obtained as 1.87 eV, is much too low in this case, reflecting the severe underestimation of the fundamental band gap. At the next level, the independent-quasiparticle approximation (IQA) includes electronic self-energy corrections within the G_0W_0 approximation that increase the band gap, resulting in a distinct blueshift of the spectrum. The bipolaron energy is now predicted to be 3.10 eV. Finally, the electron-hole attraction and local-field effects, known to be strong in LN [51,66], are taken into account by solving the Bethe-Salpeter equation. This redshifts the spectrum and places the bipolaron peak at 2.57 eV. By comparison with the IQA result, we thus deduce an electron-hole binding energy of 0.5 eV. Slightly smaller values are obtained for the other defect states considered in this work, as the electron-hole binding energy tends to decrease for shallow defect levels located closer to the conduction-band edge.

For comparison, the absorption spectrum of defect-free stoichiometric bulk LiNbO$_3$ is also displayed in Fig. 7. The smaller size of the simulation cell, which only contains 10 atoms instead of 80 atoms, allows us to include a much larger number of high-energy transitions, so that transitions up to 10 eV can be taken into account, resulting in a slower decrease of the respective absorption curve. Although the spectrum for the supercell with the embedded defect exhibits slightly smaller oscillator strengths, the peak positions as well as their general shape, including the two shoulders at around 6 eV, are already well described with the reduced number of bands. Therefore, we use this approach to determine the optical absorption spectra of the other defects. As an example, Fig. 8 displays our results for the bipolaron at the Nb_{Li} antisite in comparison to the Nb_V-V_{Li} defect pair.

TABLE IV. Absorption energies in eV for free polarons (FP), bound polarons at antisites (P@Nb$_{Li}$) and at defect pairs (P@Nb$_V$-V$_{Li}$) with axial symmetry and tilted symmetry, as well as bipolarons at antisites (B@Nb$_{Li}$) and at defect pairs (B@Nb$_V$-V$_{Li}$), calculated at different levels of theory and compared to experimental values from this work and Ref. [14].

Model	IPA	IQA	BSE	Expt.	Expt. [14]
FP (axial)	0.82	1.35	1.22		0.94
FP (tilted)	0.88	1.58	1.31		0.94
P@Nb$_{Li}$ (axial)	1.83	2.23	1.86	1.95	1.69
P@Nb$_{Li}$ (tilted)	2.01	2.38	1.97	1.95	1.69
P@Nb$_V$-V$_{Li}$ (axial)	1.57	2.50	2.07		
P@Nb$_V$-V$_{Li}$ (tilted)	1.60	2.40	2.07		
B@Nb$_{Li}$	1.73	2.90	2.40	2.70	2.50
B@Nb$_V$-V$_{Li}$	1.87	3.10	2.57	2.70	2.50

Our quantitative results for the optical absorption spectra allow us to estimate the absorption cross sections for the electron polarons studied in this work and to compare them with available experimental data: We obtain maximum cross sections of 6.36×10^{-21}, 2.69×10^{-21}, and 3.35×10^{-21} m^2 for the free polarons, the bound polarons, and the bipolarons, respectively, averaged over all models of the respective polaron type. These values are slightly larger but of the same order of magnitude as derived from time-resolved pump-multiprobe spectroscopy [67].

To further analyze the nature of the defect-related absorption peak, we relate the IPA spectra to the underlying PBEsol + U band structure. This simpler approach, unlike the more complex BSE formalism, allows a direct comparison between one-particle levels (bands) and absorption energies. In this way, we find that the relatively broad defect peak is a superposition of transitions from the single defect level (initial state) into the lowest few conduction bands, namely, Nb $4d$ states [68,69] centered around 0.2 eV above the conduction-band edge. This means that the bipolaron, once excited, is destroyed, and one of the excess electrons is no longer localized at the two involved central Nb atoms but delocalized over several Nb atoms. Within the BSE, the maximum peak energy of about 2.5 eV then implies an energy threshold of 2.3 eV, in perfect agreement with the photon energy reported for optical dissociation [22].

In Table IV, we summarize the absorption energies (maximum peak positions) calculated within IPA, IQA, and BSE for all polaron models studied here. For the models with unpaired electrons (i.e., single polarons), the values are spin corrected as described in Sec. II A. Comparing our results to the experimental data by Schirmer *et al.* [14], we note that the absorption energy for free polarons is overestimated by both the axial and the tilted configuration, for which we obtain 1.22 and 1.31 eV, respectively. The deviation from the experimental value of 0.94 eV may in part be due to the known difficulty of accurately modeling localized but weakly bound excess electrons in supercell calculations [70].

The deviations between experiment and theory are smaller for bound polarons and bipolarons. Here, we make use of our additional experimental measurements, carried out as described in Sec. II B. The resulting absorption spectrum covers
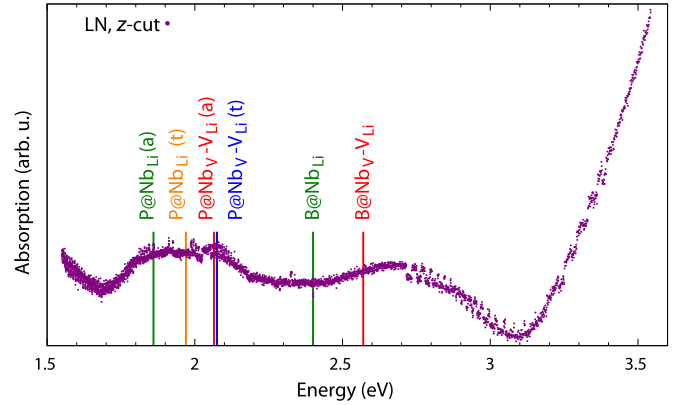

FIG. 9. Experimental absorption spectrum of congruent LiNbO$_3$ above 1.5 eV measured along the z direction using the ordinary refractive index of the material. The calculated optical absorption energies of bound polarons and bipolarons are indicated by vertical lines. For the polarons, the energies for the tilted (t) ground state and for the axial (a) configuration are included. The free-polaron signal is below the detected energy range.

the energy range between 1.5 and 3.5 eV as shown in Fig. 9. Two broad absorption maxima are visible around 1.95 and 2.7 eV, which can be attributed to polarons and bipolarons, respectively. Compared to Ref. [14], these values are slightly blueshifted. The calculated absorption energies for polarons localized at Nb$_{Li}$ antisites are in fact bracketed by the two sets of experimental data (see Table IV), while the corresponding values for Nb$_V$-V$_{Li}$ defect pairs are slightly higher than measured. A similar agreement is found for bipolarons, albeit with a tendency to slightly too low calculated values. However, the deviations are not large enough to definitely rule out any of the models studied in this work. In fact, it appears likely that different defect configurations contribute to the experimental spectra, as suggested by the broad features in Fig. 9. A superposition of the four defect peaks originating from the regular antisite and the defect pair in the axial and tilted configurations would actually explain not only the energetic position of the polaron absorption band around 1.95 eV but also its shape.

IV. CONCLUSIONS

In summary, we investigated the atomic and electronic structures as well as the spectroscopic fingerprints of polarons and bipolarons in LiNbO$_3$ by comparing theoretical simulations with measured data. We examined the following models: free polarons at regular Nb$_{Nb}^*$ atoms and bound (bi)polarons at two Nb-related point defects, the isolated Nb$_{Li}$ antisite, and the Nb$_V$-V$_{Li}$ defect pair. For the polaron (+3) and the fully ionized (+4) charge state, the defect pair is identified as a metastable configuration of the regular Nb$_{Li}$ antisite. The transition is driven by the Nb antisite atom, which can thermally overcome an energy barrier and move into a neighboring empty oxygen octahedron. For the bipolaron (charge state +2), the two configurations are even energetically equivalent, a fact that has strong implications for the charge-carrier dynamics in the material.

For both free and bound polarons, we uncover the existence of a quasi-Jahn-Teller distortion leading to tilted ground-state configurations, which transform into axial symmetry at higher temperature. Our calculated EPR parameters confirm that polarons at Nb-related defects in the tilted configuration nicely explain the experimentally observed EPR signal. Although the regular antisite fits best to the experimental data, the metastable defect pair exhibits only a minor variance and cannot be excluded with certainty. Here, future EPR measurements in the optical channel (optical detected magnetic resonance) would be beneficial for an unambiguous assignment of the EPR spectra to a specific optical transition. A similar picture emerges from the calculated optical absorption spectra: The regular antisite fits best to the polaron absorption band around 1.7 eV, but an admixture of peaks from the Nb_V-V_{Li} defect pair improves the description of the energetic position as well as the spectral shape of the absorption band as measured in this work.

For the bipolarons, on the other hand, the influence of the defect pair is clearly apparent, especially with respect to the mechanisms of bipolaron splitting and recombination. Its existence, arising from the bistability of the Nb antisite defect, provides a natural explanation not only for the experimentally observed thermal dissociation at 800 K [63] but also for the previously reported two-path recombination. While the fast process is most probably due to a direct recombination with free polarons, our results suggest that the slow process is accompanied by a structural transformation. As this transformation involves directed atomic displacements in the Nb_{Li} sublattice, it might have a strong influence on the macroscopic polarization and should be considered for an explanation of known dielectric anomalies in the material [62].

[1] A. Zaltron, G. Bettella, G. Pozza, R. Zamboni, M. Ciampolillo, N. Argiolas, C. Sada, S. Kroesen, M. Esseling, and C. Denz, Proc. SPIE **9506**, 950608 (2015).

[2] K. Hoppe, W. Fahrner, A. Petrov, D. Fink, V. Hnatowicz, J. Vacik, D. Bork, and P. Heitjans, Sens. Actuators, A **302**, 111768 (2020).

[3] S. Yin, Proc. IEEE **87**, 1962 (1999).

[4] L. Nguyen Binh, J. Cryst. Growth **288**, 180 (2006).

[5] M. Sumets, *Lithium Niobate-Based Heterostructures* (IOP, Bristol, 2018).

[6] T. Volk and M. Wöhlecke, *Lithium Niobate*, Springer Series in Materials Science Vol. 115 (Springer, Berlin, 2009).

[7] I. V. Kityk, M. Makowska-Janusik, M. D. Fontana, M. Aillerie, and F. Abdi, J. Appl. Phys. **90**, 5542 (2001); J. Phys. Chem. B **105**, 12242 (2001).

[8] P. Reichenbach, T. Kämpfe, A. Haußmann, A. Thiessen, T. Woike, R. Steudtner, L. Kocsor, Z. Szaller, L. Kovács, and L. M. Eng, Crystals **8**, 214 (2018).

[9] Y. Li, W. G. Schmidt, and S. Sanna, Phys. Rev. B **91**, 174106 (2015).

[10] U. Schlarb and K. Betzler, Phys. Rev. B **48**, 15613 (1993).

[11] M. Imlau, H. Badorreck, and C. Merschjann, Appl. Phys. Rev. **2**, 040606 (2015).

[12] L. Li, Y. Fan, Y. Li, X. Zhao, and X. Cheng, Cryst. Growth Des. **20**, 2774 (2020).

[13] S. Messerschmidt, A. Krampf, F. Freytag, M. Imlau, L. Vittadello, M. Bazzan, and G. Corradi, J. Phys.: Condens. Matter **31**, 065701 (2019).

[14] O. F. Schirmer, M. Imlau, C. Merschjann, and B. Schoke, J. Phys.: Condens. Matter **21**, 123201 (2009).

[15] R. J. Holms and W. J. Minford, Ferroelectrics **75**, 63 (1987).

[16] N. Iyi, K. Kitamura, F. Izumi, J. K. Yamamoto, T. Hayashi, H. Asano, and S. Kimura, J. Solid State Chem. **101**, 340 (1992).

[17] P. Lerner, D. Legras, and J. P. Dumas, J. Cryst. Growth **3–4**, 231 (1968).

[18] D. M. Smyth, Ferroelectrics **50**, 93 (1983).

[19] N. Zotov, H. Boysen, F. Frey, T. Metzger, and E. Born, J. Phys. Chem. Solids **55**, 145 (1994).

[20] F. Jermann, M. Simon, R. Böwer, E. Krätzig, and O. F. Schirmer, Ferroelectrics **165**, 319 (1995).

[21] P. Herth, D. Schaniel, T. Woike, T. Granzow, M. Imlau, and E. Krätzig, Phys. Rev. B **71**, 125128 (2005).

[22] C. Merschjann, D. Berben, M. Imlau, and M. Wöhlecke, Phys. Rev. Lett. **96**, 186404 (2006).

[23] O. F. Schirmer and D. von der Linde, Appl. Phys. Lett. **33**, 35 (1978).

[24] O. F. Schirmer, O. Thiemann, and M. Wöhlecke, J. Phys. Chem. Solids **52**, 185 (1991).

[25] H. Müller and O. F. Schirmer, Ferroelectrics **125**, 319 (1992).

[26] H. X. Feng, J. K. Wen, H. F. Wang, S. Y. Han, and Y. X. Xu, J. Phys. Chem. Solids **51**, 397 (1990).

[27] D. A. Dutt, F. J. Feigl, and G. G. DeLeo, J. Phys. Chem. Solids **51**, 407 (1990).

[28] H. Donnerberg, S. M. Tomlinson, C. R. A. Catlow, and O. F. Schirmer, Phys. Rev. B **40**, 11909 (1989).

[29] G. E. Peterson and A. Carnevale, J. Chem. Phys. **56**, 4848 (1972).

[30] M. Friedrich, W. G. Schmidt, A. Schindlmayr, and S. Sanna, Phys. Rev. Mater. **1**, 054406 (2017).

[31] S. Botti, A. Schindlmayr, R. Del Sole, and L. Reining, Rep. Prog. Phys. **70**, 357 (2007).

[32] P. Giannozzi *et al.*, J. Phys.: Condens. Matter **21**, 395502 (2009); https://www.quantum-espresso.org.

[33] J. P. Perdew, A. Ruzsinszky, G. I. Csonka, O. A. Vydrov, G. E. Scuseria, L. A. Constantin, X. Zhou, and K. Burke, Phys. Rev. Lett. **100**, 136406 (2008).

[34] M. Friedrich, A. Riefer, S. Sanna, W. G. Schmidt, and A. Schindlmayr, J. Phys.: Condens. Matter **27**, 385402 (2015).

[35] M. Friedrich, A. Schindlmayr, W. G. Schmidt, and S. Sanna, Phys. Status Solidi B **253**, 683 (2016).

[36] F. Schmidt, M. Landmann, E. Rauls, N. Argiolas, S. Sanna, W. G. Schmidt, and A. Schindlmayr, Adv. Mater. Sci. Eng. **2017**, 3981317 (2017).

[37] H. H. Nahm and C. H. Park, Phys. Rev. B **78**, 184108 (2008).

[38] M. Cococcioni and S. de Gironcoli, Phys. Rev. B **71**, 035105 (2005).

[39] H. Boysen and F. Altorfer, Acta Crystallogr., Sect. B **50**, 405 (1994).

[40] U. Gerstmann, Phys. Status Solidi B **248**, 1319 (2011).

[41] C. J. Pickard and F. Mauri, Phys. Rev. Lett. **88**, 086403 (2002).

[42] H. J. von Bardeleben, J. L. Cantin, U. Gerstmann, A. Scholle, S. Greulich-Weber, E. Rauls, M. Landmann, W. G. Schmidt, A. Gentils, J. Botsoa, and M. F. Barthe, Phys. Rev. Lett. **109**, 206402 (2012).

[43] P. Giannozzi *et al.*, J. Phys.: Condens. Matter **29**, 465901 (2017).

[44] C. J. Pickard and F. Mauri, Phys. Rev. B **63**, 245101 (2001).

[45] J. F. Janak, Phys. Rev. B **18**, 7165 (1978).

[46] S. Sanna, T. Frauenheim, and U. Gerstmann, Phys. Rev. B **78**, 085201 (2008).

[47] Y. Li, S. Sanna, and W. G. Schmidt, J. Chem. Phys. **140**, 234113 (2014).

[48] J. Heyd, G. E. Scuseria, and M. Ernzerhof, J. Chem. Phys. **118**, 8207 (2003).

[49] A. Riefer, M. Friedrich, S. Sanna, U. Gerstmann, A. Schindlmayr, and W. G. Schmidt, Phys. Rev. B **93**, 075205 (2016).

[50] L. Hedin, Phys. Rev. **139**, A796 (1965).

[51] A. Riefer, S. Sanna, A. Schindlmayr, and W. G. Schmidt, Phys. Rev. B **87**, 195208 (2013).

[52] F. Schmidt, A. Riefer, W. G. Schmidt, A. Schindlmayr, M. Imlau, F. Dobener, N. Mengel, S. Chatterjee, and S. Sanna, Phys. Rev. Mater. **3**, 054401 (2019).

[53] A. Marini, C. Hogan, M. Grüning, and D. Varsano, Comput. Phys. Commun. **180**, 1392 (2009).

[54] R. W. Godby and R. J. Needs, Phys. Rev. Lett. **62**, 1169 (1989).

[55] Crystal Technologies Inc., Lithium Niobate: Optical Waveguide Substrates, https://gandh.com/wp-content/uploads/2013/12/opticalWaveguide.pdf.

[56] Y. Fan, L. Li, Y. Li, X. Sun, and X. Zhao, Phys. Rev. B **99**, 035147 (2019).

[57] M. M. Hossain, Heliyon **5**, e01436 (2019).

[58] B. Etschmann, N. Ishizawa, V. Streltsov, and S. Oishi, Z. Kristallogr. **216**, 455 (2001).

[59] H. Lehnert, H. Boysen, F. Frey, A. Hewat, and P. Radaelli, Z. Kristallogr. **212**, 712 (1997).

[60] R. D. Shannon and C. T. Prewitt, Acta Crystallogr., Sect. B **25**, 925 (1969).

[61] S. C. Abrahams and P. Marsh, Acta Crystallogr., Sect. B **42**, 61 (1986).

[62] T. Granzow, Appl. Phys. Lett. **111**, 022903 (2017).

[63] J. Koppitz, O. F. Schirmer, and A. I. Kuznetsov, Europhys. Lett. **4**, 1055 (1987).

[64] C. Braun, S. Neufeld, U. Gerstmann, S. Sanna, J. Plaickner, E. Speiser, N. Esser, and W. G. Schmidt, Phys. Rev. Lett. **124**, 146802 (2020).

[65] D. Ceresoli, U. Gerstmann, A. P. Seitsonen, and F. Mauri, Phys. Rev. B **81**, 060409(R) (2010).

[66] W. G. Schmidt, M. Albrecht, S. Wippermann, S. Blankenburg, E. Rauls, F. Fuchs, C. Rödl, J. Furthmüller, and A. Hermann, Phys. Rev. B **77**, 035106 (2008).

[67] C. Merschjann, B. Schoke, D. Conradi, M. Imlau, G. Corradi, and K. Polgár, J. Phys.: Condens. Matter **21**, 015906 (2009).

[68] M. Boukhtouta, Y. Megdoud, S. Benlamari, H. Meradji, Z. Chouahda, R. Ahmed, S. Ghemid, M. Abu-Jafar, S. Syrotyuk, D. P. Rai, S. Bin Omran, and R. Khenata, Philos. Mag. **100**, 1150 (2020).

[69] R. Husin, F. W. Badrudin, M. F. M. Taib, and M. Z. A. Yahya, Mater. Res. Express **6**, 114002 (2019).

[70] A. Hermann, P. Schwerdtfeger, and W. G. Schmidt, J. Phys.: Condens. Matter **20**, 225003 (2008).